Main Manuscript for

Megathrust Earthquakes Amplify Coastal Wave Hazards in Cascadia Under Rising Sea Levels

Cesar G. Lopez[1] and Claire C. Masteller[1]
[1]Department of Earth, Environmental, and Planetary Sciences, Washington University in St. Louis, St. Louis, Missouri 63130, USA

*Corresponding Author: Cesar G. Lopez
Email: c.g.lopez@wustl.edu

Author Contributions: C.G.L and C.C.M designed the research, C.G.L developed and ran the model simulations, and C.G.L and C.C.M analyzed the results and wrote the manuscript.

This PDF file includes:

Main Text
Figures 1 to 5

Abstract

Along the Cascadia Subduction Zone, destructive megathrust earthquakes represent a significant coastal hazard. These events generate abrupt coseismic subsidence, instantaneously increasing relative sea level. In the coming decades, global sea level rise will continue to shift baseline coastal conditions, potentially enhancing earthquake-driven hazards. Here, we model how sea level rise, wave climate, and the magnitude and timing of earthquake-driven subsidence interact to influence nearshore wave dynamics along the Cascadia margin. We find that coseismic subsidence amplifies shoreline wave power by shifting wave action landward despite reductions in wave breaking. This amplification is strongly controlled by shore platform slope, with negligible increases along steep shores and up to a million-fold increase in wave power for low-gradient sites. These changes highlight the potential for drastic increases in coastal erosion following future earthquakes. The timing and persistence of these hazards strongly depend on the sea level trajectory. Under a high-emissions scenario, accelerated sea level rise shifts the window of maximum earthquake-driven wave amplification earlier in the century, increasing the potential of post-event coastal recovery. Our results demonstrate that interactions between climate and solid Earth geohazards create transient, but potentially long-lived, shifts in coastal wave energy regimes that can shape future hazards and landscape evolution.

Main Text

Introduction

The Cascadia Subduction Zone (CSZ) stretches along the Pacific Northwest coast of North America, extending from the Mendocino Triple Junction in northern California to Vancouver Island in British Columbia [1]. Formed through the subduction of the Juan de Fuca Plate beneath North America [2–4], the CSZ can generate some of the world's most powerful earthquakes [5,6], with profound consequences for communities, infrastructure, and natural hazards along the coastline [7–9].

Paleoseismic records indicate earthquake recurrence intervals of 200 to 800 years, with an average of ~500 years for the largest events [10,11], with the last large Cascadia earthquake occurring over 320 years ago in 1700 AD [12,13]. Time-dependent earthquake recurrence models indicate a 30% chance of a > M8 earthquake occurring in southern Cascadia in the next 50 years and a 10% to 15% chance of an approximately M9 rupture of the full subduction zone [14,15]. These estimates indicate that a future Cascadia earthquake is a realistic possibility within the coming century, motivating efforts to understand future coastal hazards driven by such an event.

Megathrust earthquakes generate a range of hazards, including coseismic vertical land motion. Coastal wetland stratigraphy [16–21] and geodetic modeling approaches [22–25] indicate that Cascadia earthquakes can generate 0.5 to 2 m of instantaneous subsidence along the coastline. This subsidence produces abrupt relative sea level rise (RSLR), that increases nearshore water depths [8,26]. RSLR is driven both by active tectonics and eustatic sea level rise (SLR), which is increasing in response to climate change [27–29]. Although interseismic uplift has historically buffered the effects of SLR in portions of Cascadia [30], projected rates of SLR are expected to outpace this buffering over the coming century [31,32]. By 2100, global sea levels are projected to rise by 0.56 m (0.43 to 0.76 m) relative to conditions from 1995 to 2014 under SSP2-4.5, a moderate emissions scenario. Under SSP5-8.5, a very high emissions scenario representing the upper envelope of emissions futures, sea level is projected to increase by 0.77 m (0.63 to 1.01 m). These projections are comparable to the lower bound of coseismic subsidence expected from a Cascadia earthquake. Both the emissions trajectory and the timing of the next earthquake will determine the sea level baseline upon which coseismic subsidence is superimposed.

By modulating nearshore water depths, RSLR controls the location of wave breaking and how efficiently offshore wave power (kW/m) is transmitted to the coastline, which drives erosion on rocky coasts [33,34]. Tectonically-driven vertical land motion exerts a first order control on rocky shoreline retreat by modifying cliff-front wave power [35]. Specifically, interseismic subsidence increases nearshore water depths and shifts wave breaking landward, leading to enhanced cliff front wave power and more rapid coastal retreat.

How these compounding shifts in RSL will influence rocky coast erosion remains poorly constrained. Some studies suggest that increasing nearshore water depths will propagate wave action landward, increasing cliff-front wave power and coastal erosion [36–38]. Others have argued the opposite effect, proposing that relatively deep water at the cliff base may instead suppress nearshore wave breaking, thereby reducing wave power and erosion, with responses highly dependent on local shore platform morphology [39,40]. Set against this shifting background of level rise, the response of Cascadia coastlines to a future megathrust earthquake remains highly uncertain as coseismic subsidence could either suppress or amplify coastal wave hazards.

In this contribution, we model earthquake-driven changes in nearshore wave dynamics at 32 sites across Cascadia (Fig. 1) in response to the combined effects of coseismic subsidence and global SLR. Selected sites span a range of shore platform morphologies and water levels, with many located within or near major population centers and recreational destinations. Across these sites, we explore a parameter space defined by earthquake timing (at decadal intervals), coseismic subsidence magnitude (0.5, 1.0, and 2.0 m), and century-scale trajectories of both offshore wave climate [41] and sea level rise under a moderate (SSP2-4.5) and high (SSP5-8.5), respectively. Model simulations are run in hourly time steps from 2020 to 2100.

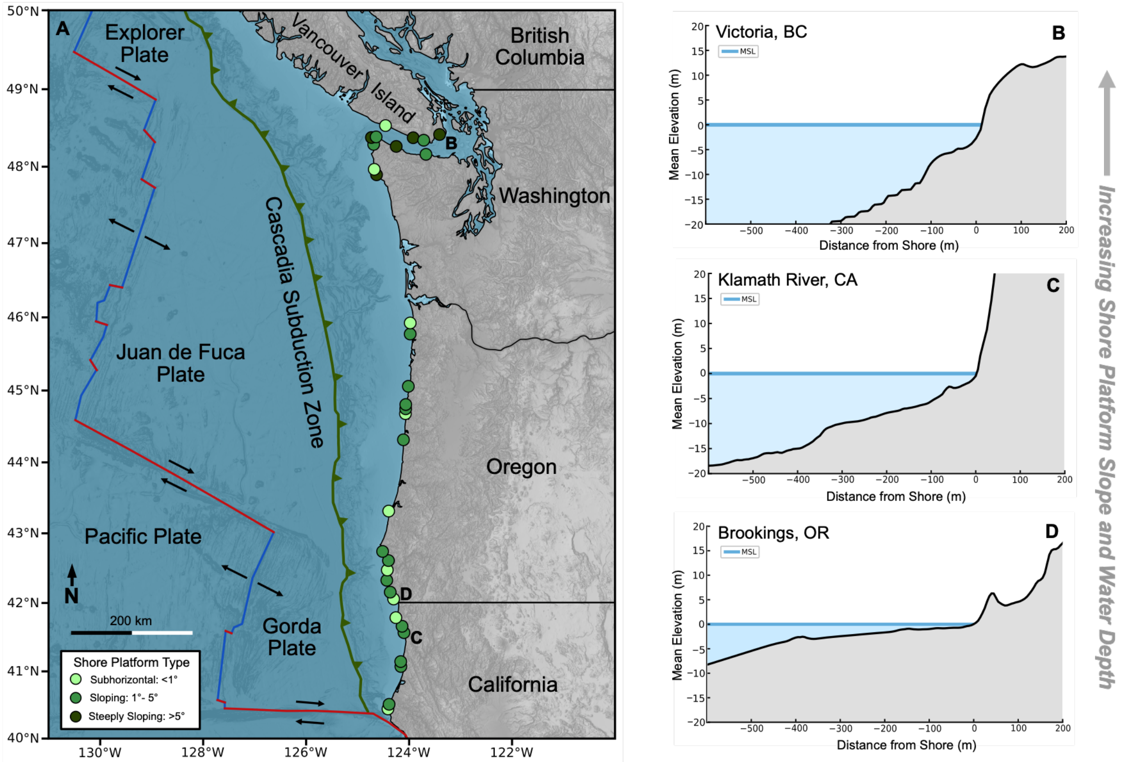

Figure 1. A) Map of Cascadia. Arrows denote tectonic plate motion direction and points represent the 32 study sites, which are classified based on the underlying shore platform slope. B-D.) Swath profiles for three of the study sites representing the three primary platform categories in order of descending slope. Site locations are denoted on the map by their respective letter.

Results

Earthquake-Driven Changes in Nearshore Dynamics

To characterize the effects of coseismic subsidence and RSLR on nearshore wave dynamics, we first classify cliff-incident waves as breaking, broken, and unbroken.[42] Breaking and broken waves drive erosion, whereas unbroken waves largely reflect from the cliff with minimal energy transfer [43]. Even in baseline scenarios without coseismic subsidence, climate-driven RSLR progressively suppresses nearshore wave breaking. By 2100, the number of breaking and broken waves declines by 8.5% to 19.8% under SSP2-4.5 relative to 2020 conditions. Under the high-emissions SSP5-8.5 scenario, this reduction increases by 8.5% to 26.7% across all sites.

Superimposed on this background trajectory, coseismic subsidence produces an additional instantaneous reduction in breaking and broken waves, with the magnitude of this reduction increasing with subsidence (Fig. 2). Across all sites, earthquake timings, and emissions scenarios, median reductions in wave breaking range from 0.1% for 0.5 m of subsidence, to 1.1% for 1.0 m, and 9.2% for 2.0 m (Fig. 2A, E). It is worth emphasizing that the reduction produced by 2.0 m of subsidence is comparable in magnitude to the wave breaking reduction accumulated over the century through SLR alone. By 2100, the maximum wave breaking reductions reach 52.0% under SSP2-4.5 and 53.4% under SSP5-8.5, approximately twice the maximum centennial-scale reduction produced by climate change.

This reduction in breaking and broken waves is accompanied by a landward migration of wave breaking (Fig. 2). By the end of the century, for baseline model scenarios, median annual offshore wave breaking distances shift landward from 0 m to 185 m under SSP2-4.5 and 5 m to 245 m for SSP5-8.5. Again, coseismic subsidence under SSP-4.5 produces an additional, instantaneous landward shift with a median magnitude from 10 m for 0.5 m of subsidence to 25 m for 1.0 m and 40 m for 2.0 m, with maximum shifts of 193 m, 330 m, and 555 m, respectively. Under SSP5-8.5, the corresponding median shifts are 12.5 m, 25 m, and 40 m, with maxima of 190 m, 325 m, and 555 m. Based on these results, the landward migration of wave breaking is substantially more sensitive to coseismic subsidence magnitude than the background emissions trajectory. Between sites, shore platform slope strongly modulates the landward shift of wave breaking (Fig. 2). Subhorizontal platforms provide an extensive shallow water zone across which breaking can shift landward as water levels rise. In contrast, steeper platforms have a narrower zone of wave transformation concentrated near the shore under baseline conditions, such that rising water levels have a reduced effect.

Increases in coseismic subsidence and RSLR also shift the size of breaking waves. For modeled earthquake scenarios, median offshore wave heights for broken and breaking waves increase by up to 48% (1.4 m) across sites and emissions scenarios. The waves that continue to break under coseismic subsidence are larger, delivering more power to the shore. Increasing coseismic subsidence also shifts the upper bounds of median breaking and broken wave heights by 9.18% (0.5 m), 19.10% (1.0 m), and 48.29% (2.0 m) across all sites and scenarios relative to baseline conditions.

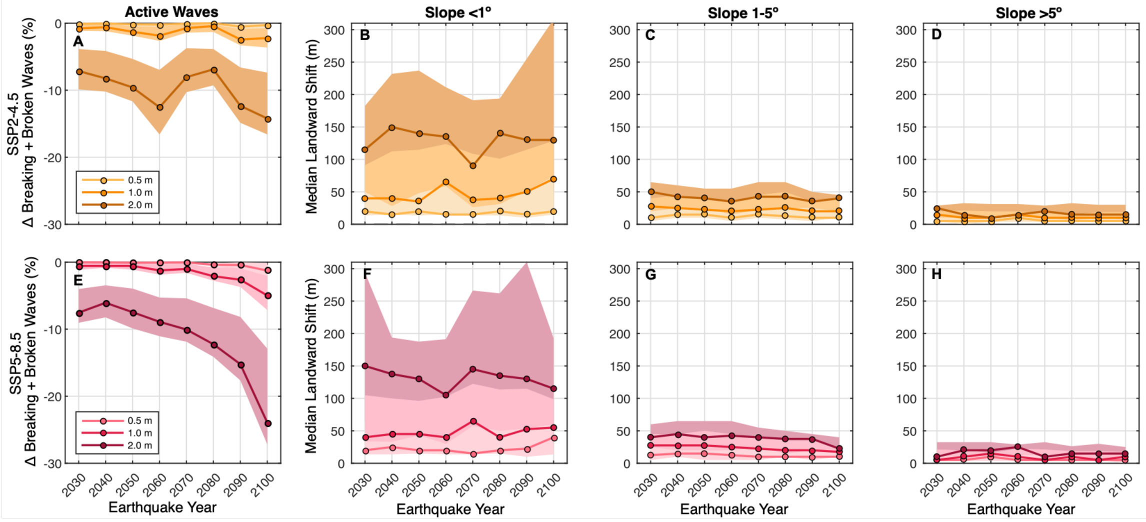

Figure 2. (A and E) Median percent change in the number of broken and breaking waves for SSP2-4.5 (A) and SS-5-8.5 (E) across each earthquake year and all sites, with shaded envelopes denoting the interquartile range. (B-D; F-H) Median landward shift in breaking distances across all sites by slope class for each modeled earthquake year for SSP2-4.5 (B-D) and SSP5-8.5 (F-H). Shaded regions denote the interquartile range.

Subsidence-Driven Amplification of Wave Power

Cliff-base wave power (P_{cliff}) is estimated for each forecast wave using a modified decay function (Methods; SI) to account for energy dissipation after breaking. The P_{cliff} estimates are then integrated over each year to calculate total annual P_{cliff}. We find that across all sites and scenarios, earthquake-driven subsidence drastically enhances shoreline wave power. To further quantify these effects, we compute an amplification factor defined as the ratio of total P_{cliff} under an earthquake scenario to that under the baseline, SLR-only scenario for the same year (Methods).

The timing of maximum wave power amplification, or the year in which a megathrust earthquake produces the greatest enhancement of P_{cliff} relative to baseline conditions, defines the upper envelope of earthquake-driven wave hazard amplification. This timing is highly variable for a given earthquake across the model period, following emission scenario-specific patterns (Fig. 3A). Under SSP2-4.5, we find bimodal behavior, with most sites achieving maximum amplification during earthquakes that occur in 2030 or 2080. In contrast, under SSP5-8.5, amplification is greatest early in the model period around 2030 or 2040 before decreasing thereafter (Fig. 3A). For 0.5 m of subsidence, 7 sites feature the same maximum amplification years between SSP2-4.5 and SSP5-8.5 while 25 sites have different amplification years, 5 sites experience the same maximum amplification year for 1.0 m of subsidence, and 8 sites for 2.0 m of subsidence. This variability emphasizes the importance of the climate scenario in controlling the timing of maximum amplification.

For modeled earthquake scenarios under both emission scenarios, maximum amplification ranges from no amplification to a millionfold increase in wave power across all sites, scenarios, and years, which corresponds to a 10^1 to 10^4 kW/m increase in total annual P_{cliff}. Overall, amplification scales with the magnitude of subsidence (Figure 3B-C). Maximum amplification spans 4 orders of magnitude for 0.5 m subsidence and 6 and 7 orders of magnitude for 1.0 m and 2.0 m of subsidence, respectively across all sites and scenarios relative to baseline, SLR-only conditions. These results demonstrate a strong coupling between baseline P_{cliff} and the scale of amplification, such that sites with lower baseline P_{cliff} have greater amplification than those that already have high P_{cliff}. This indicates a strong and predictable relationship across climate scenarios, suggesting that similar nearshore water levels set the magnitude of amplification.

Amplification also exhibits a strong dependence on shore platform morphology (Fig. 4). At each site across all model scenarios, mean P_{cliff} amplification is negatively correlated with shore platform slope (Spearman's $\rho \leq -0.91$, $p < 0.05$), indicating that earthquake-driven amplification is muted on steeper shore platforms. Further, the range of amplification decreases as slope increases, narrowing from 10^0 to 10^6 on subhorizontal shore platforms (< 1°), to a single order of magnitude on steeply sloping platforms (> 5°).

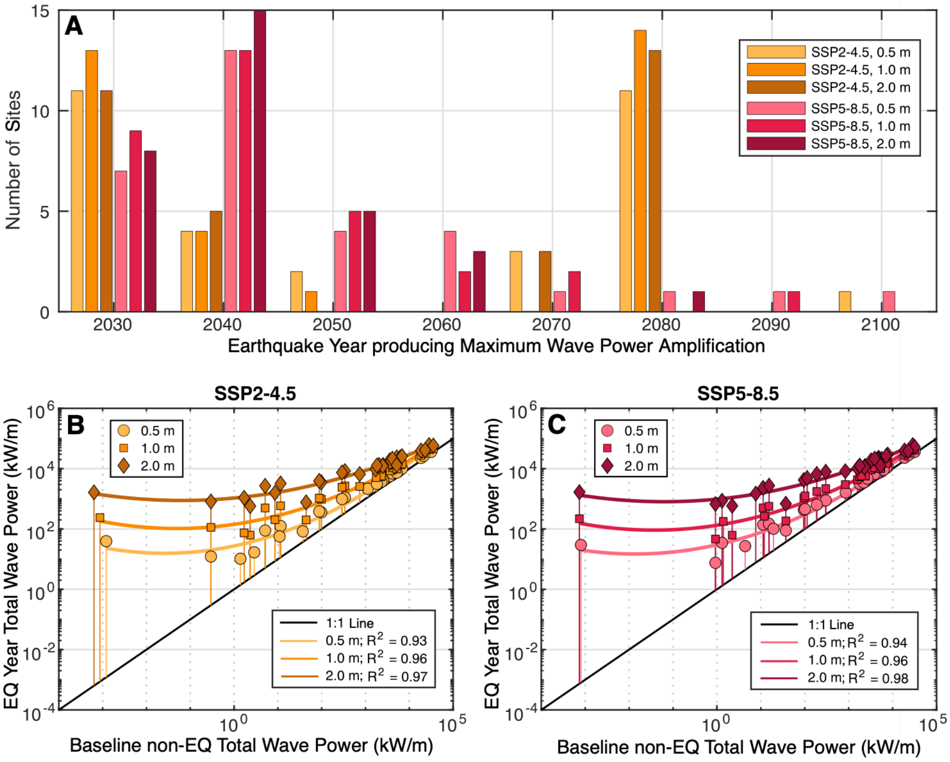

Figure 3. A) Earthquake years producing maximum amplification of wave power relative to a baseline scenarios without coseismic subsidence. B-C) Total annual P_{cliff} amplification for site-specific EQ years that maximize amplification for SSP2-4.5 (B) and SSP5-8.5 (C).

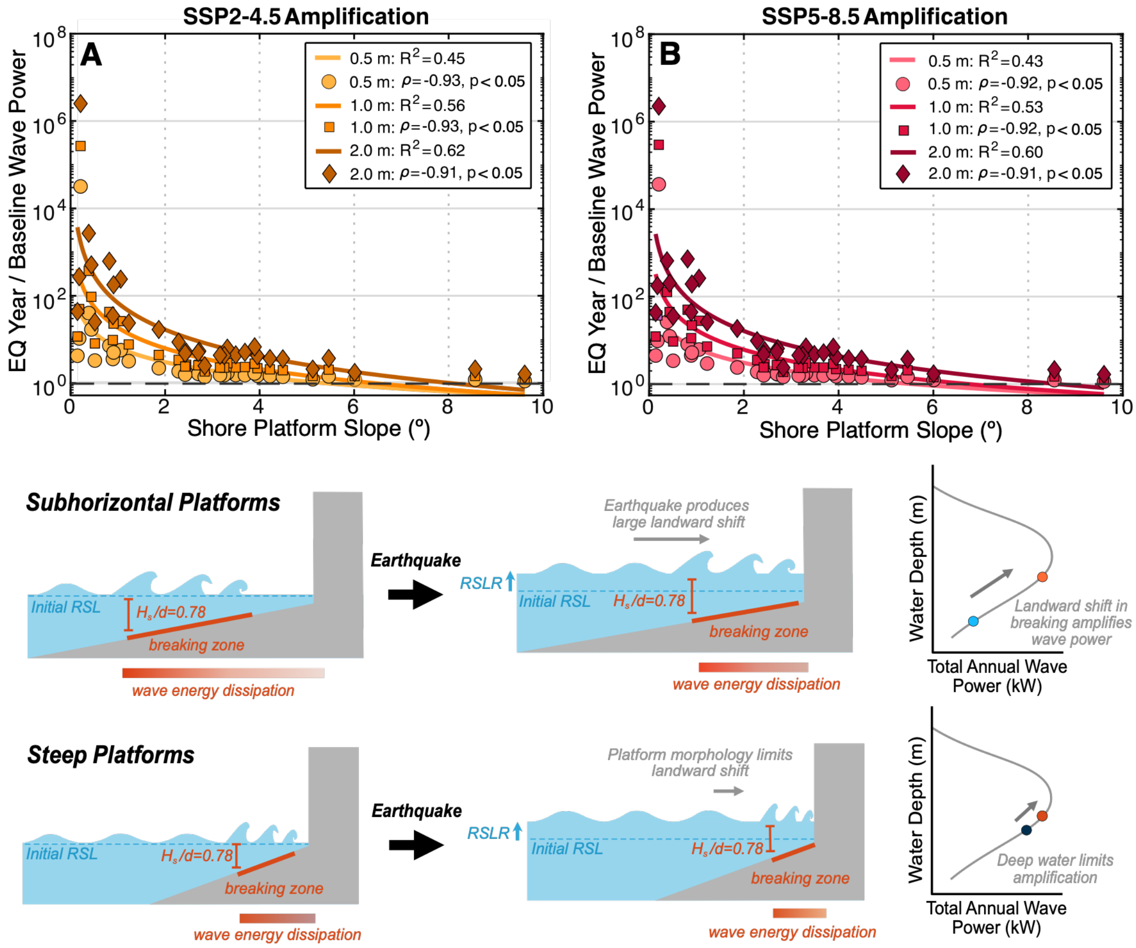

Figure 4. A-B). Total annual P_{cliff} amplification as a function of shore platform slope for site-specific EQ years that maximize wave power amplification for SSP2-4.5 (A) and SSP5-8.5(B) Bottom rows are schematic diagrams depicting the effects of earthquake-driven RSLR on nearshore wave action and P_{cliff} for subhorizonal and steep platforms.

Seismic Memory and Coastal Hazard Trajectories

Megathrust earthquake-driven increases in nearshore water levels fundamentally change the long-term trajectory of wave-energy forcing over the remainder of the century. Across all emissions-subsidence model pairings, representing 256 unique realizations, increasing coseismic subsidence systematically shifts the timing of peak total annual P_{cliff} earlier in the century (Fig 5a). Under SLR-only conditions, most simulations reach peak annual P_{cliff} at the end of the century, consistent with the increasing water depth associated with ongoing RSLR. However, as the magnitude of coseismic subsidence increases, a growing number of simulations achieve peak P_{cliff} earlier, with the largest subsidence scenarios exhibiting substantial clustering of peaks in P_{cliff} between 2070 to 2090, rather than 2100 (SI Fig 1). This indicates that coseismic subsidence shifts the timing of peak P_{cliff} earlier by effectively accelerating the increases in wave power delivery that would otherwise occur more gradually through climate-driven SLR. Importantly, the years of peak total annual P_{cliff} do not coincide with the years that maximize amplification relative to baseline conditions. Instead, peaks in P_{cliff} are the result of the combined influence of earthquake-driven subsidence and RSLR, emphasizing that coastal wave-energy delivery depends on the evolving interaction between both processes rather than on the punctuated effects of the megathrust earthquake alone.

Comparing total annual P_{cliff} in 2100 with each earthquake year across all model realizations reveals how nearshore wave dynamics continue to evolve following coseismic subsidence (Fig. 5a; SI Fig S1-2). 65.1% of model realizations experience a sustained or higher total annual P_{cliff} through 2100 following the initial earthquake. An additional 12.5% of realizations experience negligible change between the earthquake year and the end of the century. The remaining 22.4% of subsidence-emission pairing scenarios experience P_{cliff} decline following a coseismic subsidence-driven increase. These contrasting trajectories reflect the nonlinear influence of water depth on nearshore wave transformation: although initial coseismic subsidence shifts wave breaking landward and increases energy delivery to the cliff across all sites and scenarios, in some instances, continued RSLR can deepen water over the shore platform such that suppressed wave breaking can reduce P_{cliff} (Fig. 5b). In these instances, initiation of recovery is achieved, particularly for steeply sloping sites concentrated in northern Cascadia (Fig 5a) and high subsidence-emissions pairings. However, sites comprising subhorizontal platforms, scenarios under SSP2-4.5, or 0.5-1.0 m of cosismic subsidence are more likely to have permanently amplified hazard potential throughout the rest of the century.

To distinguish substantial declines in P_{cliff} from more minor year-to-year wave climate variability, we identify all model realizations in which total annual P_{cliff} decreases by at least 5% between the earthquake year and 2100 (Fig. 5C). The magnitude of the post-peak decline is quantified as the fraction of model realizations in which total annual P_{cliff} decreases by at least 5% between P_{cliff} during the earthquake year and 2100 (Fig. 5C). Under SSP2-4.5, the fraction of realizations exceeding this threshold increases from approximately 10% under 0.5 m of subsidence to 30% under 2.0 m. This sensitivity is substantially stronger under SSP5-8.5, where the fraction increases from approximately 20% to 70% across the same subsidence scenarios. These results demonstrate that more rapid late-century RSLR can progressively reverse the initial earthquake-driven amplification of P_{cliff}, making enhanced wave energy delivery increasingly transient as the magnitudes of both subsidence and subsequent sea-level rise increase.

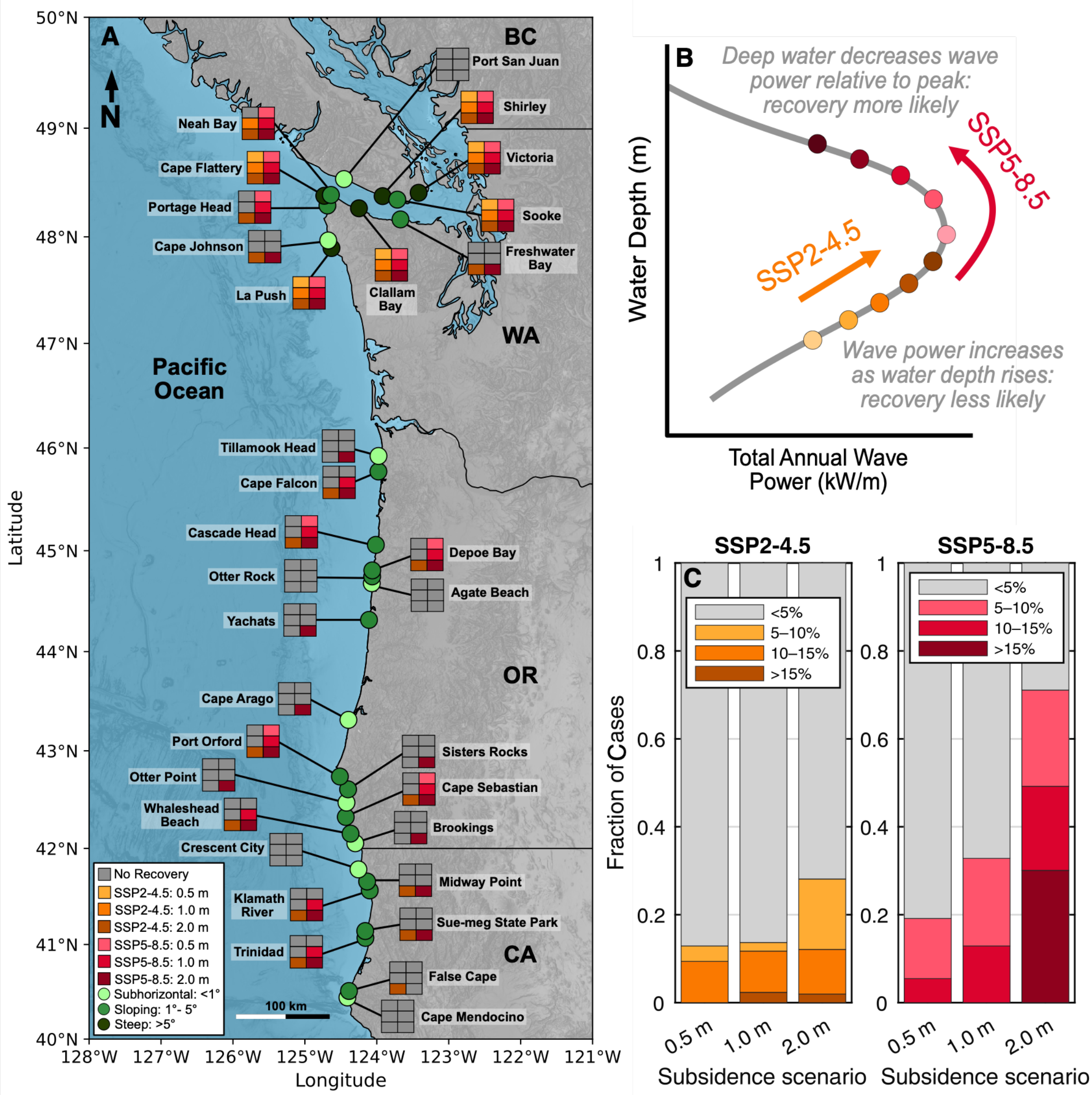

Figure 5. A) Map of study sites. Sites are denoted by the green circles, with shading indicating the shore platform slope class as in Figure 1. Grids indicate whether some recovery is achieved, with colors denoting for which emissions-subsidence pairings. Recovery occurs when peak P_{cliff} occurs for an earthquake scenario in at least one earlier decade. A gray grid-cell indicates no recovery is initialed or achieved for a specific emissions-subsidence pairings, with a fully gray grid cell denoting no recovery under all simulations for that site. (B) Schematic depiction of the effects of subsidence and SLR on P_{cliff} for each emissions scenario. C) Fraction of model runs where P_{cliff} is reduced by 5% or more from peak total annual P_{cliff}, by subsidence scenario.

Discussion

Coseismic Subsidence and Sea Level Effects on Coastal Processes

Increasing coseismic subsidence and RSL decreases wave breaking in the nearshore (Fig. 2). These results agree with past studies [40] which find that as sea level rises, wave breaking decreases, suggesting reduced energy transfer to the shore and likely less erosion. Megathrust earthquake-driven subsidence leads to instant hydrodynamic transitions, where water depth at the cliff-base becomes sufficiently deep to turn off wave breaking for some percentage of incident waves. At face value, this would suggest reduced energy at the cliff and therefore likely less erosion. The resulting increase in water depth also produces an immediate landward migration of wave breaking. The magnitude of the shift reflects the interaction between coseismic subsidence and shore-platform slope, where greater subsidence produces greater shifts in nearshore water depth. Gently sloping platforms translate this shift into a much larger landward migration of wave breaking relative to steeply sloping platforms.

However, model simulations show that P_{cliff} increases with coseismic subsidence and RSLR despite the reduction in wave breaking. This apparent contradiction reflects a competition between two effects: the loss of waves from the breaking-wave population and the landward migration of the waves that continue to break. Increasing water depth preferentially suppresses the breaking of smaller, lower-energy waves. At the same time, larger waves continue to break but do so progressively closer to the coastline. Because these waves traverse a shorter distance after breaking, they dissipate less energy. This reduction in energy loss outweighs the removal of smaller waves from the breaking-wave population, producing a net increase in total P_{cliff}.

Emissions Trajectory and Wave Hazard Amplification

Our results suggest an earthquake-climate coupling that governs the timing of maximum wave power amplification and peak P_{cliff}. Coseismic subsidence drives abrupt increase in water depth, but the emissions-dependent sea-level trajectory determines when this perturbation produces the window of maximum P_{cliff} amplification (Fig. 3) and whether some amount of recovery can occur (Figure 5). Under SSP5-8.5, rapid sea-level rise initially promotes greater energy delivery and hazard amplification but also advances the transition to suppressed wave breaking and reductions in P_{cliff}. Consequently, the window of maximum earthquake-driven amplification occurs earlier under SSP5-8.5 than under SSP2-4.5, revealing that identical earthquakes may produce significantly different impacts depending on the background sea level and climate state.

High emissions shifts the period of maximum earthquake-driven coastal hazards earlier, as rising sea levels diminish the relative impact of earthquakes occurring near the end of the century. Following a megathrust earthquake, our results show that continued sea level rise can drive a partial recovery of the nearshore wave climate as progressive deepening suppresses wave breaking and reduces the initial amplification of P_{cliff}, especially under SSP5-8.5. It is important to note, however, that SSP5-8.5 is increasingly regarded as a relatively unlikely climate future [44,45]. By contrast, SSP2-4.5 produces a more variable response across sites, a lower likelihood of nearshore recovery, and less predictable impacts for earthquakes occurring at different times.

Further, the reduced P_{cliff} amplification under a high emissions future should not be interpreted as a reduction in overall coastal hazard. The same increases in water depth that suppress wave breaking and promote post-earthquake recovery also increase exposure to coastal inundation [8,46,47]. The apparent recovery of P_{cliff} more likely represents a redistribution of coastal hazards rather than a return to pre-earthquake conditions.

The Legacy of Megathrust Earthquakes: Implications for Coastal Erosion and Future Hazards

Coastal erosion and retreat are regulated by the wave power delivered to the shore. Consequently, on rocky coasts, increases in P_{cliff} driven by coseismic subsidence and RSLR are expected to enhance coastal erosion. However, increases in erosion are unlikely to be spatially uniform across the region because local shore platform morphology strongly regulates the magnitude of amplification and whether recovery is attainable. The exact magnitude of potential cliff retreat remains exceedingly challenging to predict[48–50]. Measured shoreline retreat rates in the region [51–53] and previously observed scaling relationships between wave power and erosion rates [33,34], strongly suggest that multiple order of magnitude increases in P_{cliff} are likely to accelerate cliff retreat, especially on sub-horizontal and low sloping sites. This is especially consequential in Cascadia, where coastal communities and critical infrastructure are commonly concentrated along or immediately landward of eroding cliffs. Earthquake-driven increases in wave forcing could therefore compound the immediate effects of ground shaking and tsunami inundation with elevated erosion hazards that persists for decades.

While this study specifically focuses on Cascadia, the solid Earth-climate coupling we identify has global implications for hazards along tectonically active margins. The framework developed here provides a basis for predicting where earthquakes will produce sustained erosion, transient amplification followed by recovery, or an immediate reduction in wave attack following uplift. Accordingly, hazard management and planning should incorporate the potential effects of these multi-hazards to ensure proper preparedness and response not only in the immediate aftermath of an earthquake, but in the decades that follow.

Methods

To evaluate the integrated and varying effects of coseismic subsidence and RSLR on nearshore wave dynamics, we select 32 sites comprising rocky cliffs and bluffs across the length of the CSZ (Fig. 1) dominated by offshore deepwater wave climates [54,55]. Hourly model simulations are run from 2020 – 2100 for two climate scenarios; SSP2-4.5 and SSP5-8.5, which provide lower and upper bounds corresponding to intermediate and high trajectories. These scenarios were selected because SSP2-4.5 represents the lower limit of likely emissions trajectories while SSP5-8.5 serves as an extreme, high-emissions upper bound [56].

We utilize IPCC AR6 regional, medium-confidence sea level projections for the corresponding emissions scenarios in this study. We adopt the 50th percentile projections and extract the nearest sea level curve for each study site from the underlying 1° resolution dataset [56–58]. The accumulation of strain along the coupled zone of the fault during the interseismic period drives vertical land motion, with additional contributions and effects from glacial isostatic adjustment and fault creep at depth [59–62]. The combined effect of these processes are expressed in vertical land motion rates derived from local tide gauge sea level records, which also account for eustatic sea level trends [63]. Annual rates are converted to hourly rates and applied at each model time-step. Because we independently account for this deformation in the model, we use sea level curves from which the vertical land motion contributions have been removed to avoid overestimating these effects.

Tidal influences on coastal water levels are accounted for by incorporating predicted hourly water levels referenced to a mean sea level datum derived from harmonic analysis at the nearest tidal station for each site for the model period .

Offshore wave power is determined for each site from hourly 1° deep-water wave forecasts of significant wave heights and energy periods for the corresponding RCP emission scenario [41]. To account for local nearshore morphology and energy dissipation, we extract 1/2 km wide swath profiles along the prevailing wave direction from 1/3 arc-second resolution bathymetric data sets which we interpolate to a 5m resolution [65]. Linear wave theory is subsequently utilized to model wave transformations associated with shallow-water propagation to identify where conditions for the depth-dependent breaking criterion ($\gamma = 0.78$) are satisfied for the entire distribution of forecast wave measurements (SI).

Based on the water level that coincides with shore incident waves and their breaking distance relative to the coastal cliff, waves can be classified based on impact type (breaking, broken, or unbroken) in accordance with Matsumoto et al., 2024. Breaking waves transfer the most energy because they break right at the cliff, while the amount of energy or power delivered by broken waves depends on the offshore breaking distance, which is modulated by wave size, coastal morphology, and cliff-base water levels. For unbroken waves, we assume negligible cliff wave power because these waves are reflected off the cliff face without breaking [43,66]. Additionally, cliff-base wave power is estimated using a modified decay function [67–69]:

$$P_{cliff} = P_{breaking} e^{-k \cdot d} \qquad (1)$$

Where k (m^{-1}) is an attenuation constant, representing the wave dissipation rate and d is the wave breaking distance, defined at the position where depth-dependent breaking criterion is met. Three different constants are utilized (0.01, 0.05, 0.1), for each cliff wave power calculation, representing low, medium, and high attenuation respectively.

We systematically vary both the magnitude (0.5 m, 1.0 m, and 2.0 m) and timing (2030, 2040, 2050, 2060, 2070, 2080, 2090, and 2100) of coseismic subsidence. In addition, we include a control scenario without earthquake-induced subsidence to isolate the effects of RSLR in the absence of coseismic deformation. Earthquake driven subsidence (or lack thereof) is the only differentiating factor between these scenarios, all other processes and model inputs remain the same, thus the baseline, SLR-only scenario still accounts for interseismic VLM.

These model simulations are conducted for both emission scenarios at each study site. We run a total of 25 different simulations for each site per climate scenario for 1600 total model runs (800 runs across each climate scenario).

To quantify the effects of earthquake driven subsidence relative to the scenario without any coseismic subsidence, we calculate a wave power amplification factor (-). This is a ratio between the total annual P_{cliff} of a given year for a scenario with an earthquake and the same metric for the same year but for a baseline, SLR-only scenario:

$$Amplification\ Factor = \frac{Total\ Annual\ P_{cliff}\ for\ EQ\ Scenario}{Baseline\ SLR\ only\ Total\ Annual\ P_{cliff}}$$

Our model assumes that wave energy is conserved up to the point of breaking, neglecting dissipation during shoaling, as the majority of energy loss occurs during the breaking process [70–72]. Additionally, we do not incorporate shallow-water processes such as wave setup, reflection, or refraction. This simplification reflects our primary objective of isolating and characterizing the effects of RSLR on nearshore energy transfer, rather than to comprehensively model all aspects of shallow-water wave dynamics. This approach is consistent with prior wave modeling studies. The model also does not account for any changes to coastal morphology other than vertical movement of the cross-shore profile. Given the short timescale of the model simulations (80 years), the fact that we do not estimate coastal erosion rates, and the lithological composition of our study sites, this is a reasonable choice. Nonetheless, events like cliff failure or rapid shoreline retreat could lead to changes in cliff-base wave energy regimes which the model cannot account for.

Competing interests: The authors declare no competing interest.

Data, Materials, and Software Availability

All data produced are publicly available through Zenodo. *Note to Editor and Reviewers – All data will be made publicly available on Zenodo, however, the data are not yet formally published with a DOI. The formally published data will be cited here and linked with a DOI following review. This delay is to enable edits to the dataset if substantive methodological changes are suggested during the review process resulting in material changes to the data.*

References

1. Bostock, M. G., Christensen, N. I. & Peacock, S. M. Seismicity in Cascadia. *Lithos* **332–333**, 55–66 (2019).
2. Chaytor, J. D., Goldfinger, C., Dziak, R. P. & Fox, C. G. Active deformation of the Gorda plate: Constraining deformation models with new geophysical data. *Geol* **32**, 353 (2004).
3. Gulick, S. P. S., Meltzer, A. S., Henstock, T. J. & Levander, A. Internal deformation of the southern Gorda plate: Fragmentation of a weak plate near the Mendocino triple junction. *Geol* **29**, 691 (2001).
4. McCrory, P. A., Blair, J. L., Waldhauser, F. & Oppenheimer, D. H. Juan de Fuca slab geometry and its relation to Wadati-Benioff zone seismicity. *J. Geophys. Res.* **117**, 2012JB009407 (2012).
5. Walton, M. A. L. *et al.* Toward an Integrative Geological and Geophysical View of Cascadia Subduction Zone Earthquakes. *Annual Review of Earth and Planetary Sciences* vol. 49 367–398 (2021).
6. Bilek, S. L. & Lay, T. Subduction zone megathrust earthquakes. *Geosphere* **14**, 1468–1500 (2018).
7. Petersen, M. D., Cramer, C. H. & Frankel, A. D. Simulations of Seismic Hazard for the Pacific Northwest of the United States from Earthquakes Associated with the Cascadia Subduction Zone. *Pure and Applied Geophysics* **159**, 2147–2168 (2002).
8. Dura, T. *et al.* Increased flood exposure in the Pacific Northwest following earthquake-driven subsidence and sea-level rise. *Proc. Natl. Acad. Sci. U.S.A.* **122**, e2424659122 (2025).
9. Heaton, T. H. & Hartzell, S. H. Earthquake Hazards on the Cascadia Subduction Zone. *Science* **236**, 162–168 (1987).

10. Goldfinger, C. *et al.* The importance of site selection, sediment supply, and hydrodynamics: A case study of submarine paleoseismology on the northern Cascadia margin, Washington USA. *Marine Geology* **384**, 4–46 (2017).

11. Nelson, A. R. *et al.* A maximum rupture model for the central and southern Cascadia subduction zone—reassessing ages for coastal evidence of megathrust earthquakes and tsunamis. *Quaternary Science Reviews* **261**, 106922 (2021).

12. Jacoby, G. C., Bunker, D. E. & Benson, B. E. Tree-ring evidence for an A.D. 1700 Cascadia earthquake in Washington and northern Oregon. *Geol* **25**, 999 (1997).

13. Satake, K., Shimazaki, K., Tsuji, Y. & Ueda, K. Time and size of a giant earthquake in Cascadia inferred from Japanese tsunami records of January 1700. *Nature* **379**, 246–249 (1996).

14. Petersen, M. D. *et al.* The 2018 update of the US National Seismic Hazard Model: Overview of model and implications. *Earthquake Spectra* **36**, 5–41 (2020).

15. Wirth, E. A. *et al. Earthquake Probabilities and Hazards in the U.S. Pacific Northwest*. (2025) doi:https://doi.org/10.3133/fs20253050.

16. Atwater, B. F. Evidence for Great Holocene Earthquakes Along the Outer Coast of Washington State. *Science* **236**, 942–944 (1987).

17. Hawkes, A. D., Horton, B. P., Nelson, A. R., Vane, C. H. & Sawai, Y. Coastal subsidence in Oregon, USA, during the giant Cascadia earthquake of AD 1700. *Quaternary Science Reviews* **30**, 364–376 (2011).

18. Kemp, A. C., Cahill, N., Engelhart, S. E., Hawkes, A. D. & Wang, K. Revising Estimates of Spatially Variable Subsidence during the A.D. 1700 Cascadia Earthquake Using a Bayesian Foraminiferal Transfer Function. *Bulletin of the Seismological Society of America* **108**, 654–673 (2018).

19. Leonard, L. J., Currie, C. A., Mazzotti, S. & Hyndman, R. D. Rupture area and displacement of past Cascadia great earthquakes from coastal coseismic subsidence. *Geological Society of America Bulletin* **122**, 2079–2096 (2010).

20. Leonard, L. J., Hyndman, R. D. & Mazzotti, S. Coseismic subsidence in the 1700 great Cascadia earthquake: Coastal estimates versus elastic dislocation models. *Geo. Society Am. Bull.* **116**, 655 (2004).

21. Nelson, A. R., Shennan, I. & Long, A. J. Identifying coseismic subsidence in tidal-wetland stratigraphic sequences at the Cascadia subduction zone of western North America. *J. Geophys. Res.* **101**, 6115–6135 (1996).

22. Dunham, A. M. *et al.* The Impact of 3D Structure on Coseismic Coastal Land-Level Change and Tsunami Generation in the Cascadia Subduction Zone. *Geophysical Research Letters* **52**, e2025GL117783 (2025).

23. Melgar, D. Was the January 26th, 1700 Cascadia Earthquake Part of a Rupture Sequence? *JGR Solid Earth* **126**, e2021JB021822 (2021).

24. Small, D. T. & Melgar, D. Geodetic Coupling Models as Constraints on Stochastic Earthquake Ruptures: An Example Application to PTHA in Cascadia. *JGR Solid Earth* **126**, e2020JB021149 (2021).

25. Wirth, E. A. & Frankel, A. D. Impact of Down-Dip Rupture Limit and High-Stress Drop Subevents on Coseismic Land-Level Change during Cascadia Megathrust Earthquakes. *Bulletin of the Seismological Society of America* **109**, 2187–2197 (2019).

26. Melini, D. *et al.* Earthquakes and relative sealevel changes. *Geophysical Research Letters* **31**, 2003GL019347 (2004).

27. Frederikse, T. *et al.* The causes of sea-level rise since 1900. *Nature* **584**, 393–397 (2020).

28. Hamlington, B. D. *et al.* The rate of global sea level rise doubled during the past three decades. *Commun Earth Environ* **5**, 601 (2024).

29. Nerem, R. S. *et al.* Climate-change–driven accelerated sea-level rise detected in the altimeter era. *Proc. Natl. Acad. Sci. U.S.A.* **115**, 2022–2025 (2018).

30. Komar, P. D., Allan*, J. C. & Ruggiero, P. Sea Level Variations along the U.S. Pacific Northwest Coast: Tectonic and Climate Controls. *Journal of Coastal Research* **276**, 808–823 (2011).

31. Intergovernmental Panel On Climate Change (Ipcc). *The Ocean and Cryosphere in a Changing Climate: Special Report of the Intergovernmental Panel on Climate Change*. (Cambridge University Press, 2022). doi:10.1017/9781009157964.

32. Intergovernmental Panel On Climate Change (Ipcc). *Climate Change 2021 – The Physical Science Basis: Working Group I Contribution to the Sixth Assessment Report of the Intergovernmental Panel on Climate Change*. (Cambridge University Press, 2023). doi:10.1017/9781009157896.

33. Alessio, P. & Keller, E. A. Short-term patterns and processes of coastal cliff erosion in Santa Barbara, California. *Geomorphology* **353**, 106994 (2020).

34. Huppert, K. L., Perron, J. T. & Ashton, A. D. The influence of wave power on bedrock sea-cliff erosion in the Hawaiian Islands. *Geology* **48**, 499–503 (2020).

35. Lopez, C. G. & Masteller, C. C. Tectonics as a Regulator of Shoreline Retreat and Rocky Coast Evolution Across Timescales. *AGU Advances* **7**, e2025AV002065 (2026).

36. Limber, P. W., Barnard, P. L., Vitousek, S. & Erikson, L. H. A Model Ensemble for Projecting Multidecadal Coastal Cliff Retreat During the 21st Century. *JGR Earth Surface* **123**, 1566–1589 (2018).

37. Shadrick, J. R. *et al.* Sea-level rise will likely accelerate rock coast cliff retreat rates. *Nat Commun* **13**, 7005 (2022).

38. Trenhaile, A. S. Predicting the response of hard and soft rock coasts to changes in sea level and wave height. *Climatic Change* **109**, 599–615 (2011).

39. Dickson, M. E. *et al.* Sea-level rise may not uniformly accelerate cliff erosion rates. *Nat Commun* **14**, 8485 (2023).

40. Matsumoto, H., Dickson, M. E., Stephenson, W. J., Thompson, C. F. & Young, A. P. Modeling future cliff-front waves during sea level rise and implications for coastal cliff retreat rates. *Sci Rep* **14**, 7810 (2024).
41. Bricheno, L. M. & Wolf, J. RisesAM-OceanWaves: An hourly simulation of sea surface waves for historic and future climate. NERC EDS British Oceanographic Data Centre NOC (2023).
42. Matsumoto, H., Dickson, M. E., Stephenson, W. J., Thompson, C. F. & Young, A. P. Modeling future cliff-front waves during sea level rise and implications for coastal cliff retreat rates. *Sci Rep* **14**, 7810 (2024).
43. Thompson, C. F., Young, A. P. & Dickson, M. E. Wave impacts on coastal cliffs: Do bigger waves drive greater ground motion? *Earth Surface Processes and Landforms* **44**, 2849–2860 (2019).
44. Sarofim, M. C. *et al.* High radiative forcing climate scenario relevance analyzed with a ten-million-member ensemble. *Nat Commun* **15**, 8185 (2024).
45. Scafetta, N. Impacts and risks of "realistic" global warming projections for the 21st century. *Geoscience Frontiers* **15**, 101774 (2024).
46. Kirezci, E. *et al.* Projections of global-scale extreme sea levels and resulting episodic coastal flooding over the 21st Century. *Sci Rep* **10**, 11629 (2020).
47. Hinkel, J. *et al.* Coastal flood damage and adaptation costs under 21st century sea-level rise. *Proc. Natl. Acad. Sci. U.S.A.* **111**, 3292–3297 (2014).
48. Adams, P. N., Storlazzi, C. D. & Anderson, R. S. Nearshore wave-induced cyclical flexing of sea cliffs. *J. Geophys. Res.* **110**, 2004JF000217 (2005).
49. Letortu, P., Costa, S., Cador, J., Coinaud, C. & Cantat, O. Statistical and empirical analyses of the triggers of coastal chalk cliff failure. *Earth Surf Processes Landf* **40**, 1371–1386 (2015).
50. Rosser, N. J., Brain, M. J., Petley, D. N., Lim, M. & Norman, E. C. Coastline retreat via progressive failure of rocky coastal cliffs. *Geology* **41**, 939–942 (2013).

51. Hapke, C. J. & Reid, D. *National Assessment of Shoreline Change Part 4: Historical Coastal Cliff Retreat along the California Coast*. (2007).

52. Priest, G. R. Coastal Shoreline Change Study Northern and Central Lincoln County, Oregon. *Journal of Coastal Research* 140–157 (1999).

53. Ruggiero, P. *et al. National Assessment of Shoreline Change: Historical Shoreline Change along the Pacific Northwest Coast*. (2013).

54. Tillotson, K. & Komar, P. D. The Wave Climate of the Pacific Northwest (Oregon and Washington): A Comparison of Data Sources. *Journal of Coastal Research* **13**, 440–452 (1997).

55. Yang, Z. *et al.* Modeling analysis of the swell and wind-sea climate in the Salish Sea. *Estuarine, Coastal and Shelf Science* **224**, 289–300 (2019).

56. Intergovernmental Panel On Climate Change (Ipcc). *Climate Change 2021 – The Physical Science Basis: Working Group I Contribution to the Sixth Assessment Report of the Intergovernmental Panel on Climate Change*. (Cambridge University Press, 2023). doi:10.1017/9781009157896.

57. Garner, G. G. *et al.* IPCC AR6 Sea Level Projections. Zenodo https://doi.org/10.5281/ZENODO.5914709 (2021).

58. Kopp, R. E. *et al.* The Framework for Assessing Changes To Sea-level (FACTS) v1.0: a platform for characterizing parametric and structural uncertainty in future global, relative, and extreme sea-level change. *Geosci. Model Dev.* **16**, 7461–7489 (2023).

59. Burgette, R. J., Weldon, R. J. & Schmidt, D. A. Interseismic uplift rates for western Oregon and along-strike variation in locking on the Cascadia subduction zone. *J. Geophys. Res.* **114**, 2008JB005679 (2009).

60. Clark, J., Mitrovica, J. X. & Latychev, K. Glacial isostatic adjustment in central Cascadia: Insights from three-dimensional Earth modeling. *Geology* **47**, 295–298 (2019).

61. Schmalzle, G. M., McCaffrey, R. & Creager, K. C. Central Cascadia subduction zone creep. *Geochem. Geophys. Geosyst.* **15**, 1515–1532 (2014).

62. Stanton, K. M., Crider, J. G., Kelsey, H. M. & Feathers, J. K. The signature of accumulated permanent uplift, northern Cascadia subduction zone. *Quat. res.* **117**, 98–118 (2024).

63. Zervas, C. E., Gill, S. K. & Sweet, W. (William V. Estimating vertical land motion from long-term tide gauge records. https://repository.library.noaa.gov/view/noaa/14751 (2013).

64. NOAA Tides and Currents. https://tidesandcurrents.noaa.gov/.

65. NOAA National Centers for Environmental Information. Coastal Relief Models (CRMs). NOAA National Centers for Environmental Information https://doi.org/10.25921/5ZN5-KN44 (2023).

66. Bullock, G. N., Obhrai, C., Peregrine, D. H. & Bredmose, H. Violent breaking wave impacts. Part 1: Results from large-scale regular wave tests on vertical and sloping walls. *Coastal Engineering* **54**, 602–617 (2007).

67. Trenhaile, A. S. Modeling the development of wave-cut shore platforms. *Marine Geology* **166**, 163–178 (2000).

68. Trenhaile, A. Modelling the development of dynamic equilibrium on shore platforms. *Marine Geology* **427**, 106227 (2020).

69. Arróspide, C., Carrillo, H., Aguilar, G. & Cienfuegos, R. A numerical model for wave erosion spatial variability at a Headland-Bay scale on rock coasts: Development and testing with synthetic and measured bathymetries. *Marine Geology* **489**, 107634 (2025).

70. Babanin, A. V., Tsagareli, K. N., Young, I. R. & Walker, D. J. Numerical Investigation of Spectral Evolution of Wind Waves. Part II: Dissipation Term and Evolution Tests. *Journal of Physical Oceanography* **40**, 667–683 (2010).

71. Gemmrich, J. R., Mudge, T. D. & Polonichko, V. D. On the Energy Input from Wind to Surface Waves. *J. Phys. Oceanogr.* **24**, 2413–2417 (1994).

72. Iafrati, A. Energy dissipation mechanisms in wave breaking processes: Spilling and highly aerated plunging breaking events. *J. Geophys. Res.* **116**, 2011JC007038 (2011).

73. Matsumoto, H., Dickson, M. E. & Kench, P. S. Modelling the Development of Varied Shore Profile Geometry on Rocky Coasts. *Journal of Coastal Research* **75**, 597–601 (2016).